

## Heterogeneous integration of amorphous silicon carbide on thin film lithium niobate

Li, Zizheng; Sharma, Naresh; Lopez-Rodriguez, Bruno; van der Kolk, Roald; Scholte, Thomas; Voncken, Hugo; van der Boom, Jasper; Gröblacher, Simon; Zadeh, Iman Esmaeil

**DOI**

[10.1063/5.0228408](https://doi.org/10.1063/5.0228408)

**Publication date**

2025

**Document Version**

Final published version

**Published in**

APL Photonics

**Citation (APA)**

Li, Z., Sharma, N., Lopez-Rodriguez, B., van der Kolk, R., Scholte, T., Voncken, H., van der Boom, J., Gröblacher, S., & Zadeh, I. E. (2025). Heterogeneous integration of amorphous silicon carbide on thin film lithium niobate. *APL Photonics*, *10*(1), Article 016120. <https://doi.org/10.1063/5.0228408>

**Important note**

To cite this publication, please use the final published version (if applicable).  
Please check the document version above.

**Copyright**






Other than for strictly personal use, it is not permitted to download, forward or distribute the text or part of it, without the consent of the author(s) and/or copyright holder(s), unless the work is under an open content license such as Creative Commons.

**Takedown policy**

Please contact us and provide details if you believe this document breaches copyrights.  
We will remove access to the work immediately and investigate your claim.

RESEARCH ARTICLE | JANUARY 29 2025

# Heterogeneous integration of amorphous silicon carbide on thin film lithium niobate

Zizheng Li ; Naresh Sharma ; Bruno Lopez-Rodriguez ; Roald van der Kolk ; Thomas Scholte ; Hugo Voncken ; Jasper van der Boom; Simon Gröblacher ; Iman Esmail Zadeh 



*APL Photonics* 10, 016120 (2025)

<https://doi.org/10.1063/5.0228408>



View  
Online



Export  
Citation



APL Photonics

Special Topics Open  
for Submissions

[Learn More](#)

# Heterogeneous integration of amorphous silicon carbide on thin film lithium niobate

Cite as: APL Photon. 10, 016120 (2025); doi: 10.1063/5.0228408

Submitted: 12 July 2024 • Accepted: 8 January 2025 •

Published Online: 29 January 2025



Zizheng Li,<sup>1,a)</sup>  Naresh Sharma,<sup>1</sup>  Bruno Lopez-Rodriguez,<sup>1</sup>  Roald van der Kolk,<sup>1</sup>  Thomas Scholte,<sup>1</sup>   
Hugo Voncken,<sup>1</sup>  Jasper van der Boom,<sup>1</sup> Simon Gröblacher,<sup>2</sup>  and Iman Esmaeil Zadeh<sup>1</sup> 

## AFFILIATIONS

<sup>1</sup>Department of Imaging Physics (ImPhys), Faculty of Applied Sciences, Delft University of Technology, Delft 2628 CJ, The Netherlands

<sup>2</sup>Department of Quantum Nanoscience, Faculty of Applied Sciences, Delft University of Technology, Delft 2628 CJ, The Netherlands

<sup>a)</sup> Author to whom correspondence should be addressed: z.li-1@tudelft.nl

## ABSTRACT

In the past decade, lithium niobate (LiNbO<sub>3</sub> or LN) photonics, thanks to its heat-free and fast electro-optical modulation, second-order non-linearities, and low-loss, has been extensively investigated. Despite numerous demonstrations of high-performance LN photonics, processing lithium niobate remains challenging and suffers from incompatibilities with standard complementary metal-oxide-semiconductor (CMOS) fabrication lines, limiting its scalability. Silicon carbide (SiC) is an emerging material platform with a high refractive index, a large non-linear Kerr coefficient, and a promising candidate for heterogeneous integration with LN photonics. Current approaches of SiC/LN integration require transfer-bonding techniques, which are time-consuming, expensive, and lack precision in layer thickness. Here, we show that amorphous silicon carbide (a-SiC), deposited using inductively coupled plasma enhanced chemical vapor deposition at low temperatures (<165 °C), can be conveniently integrated with LiNbO<sub>3</sub> and processed to form high-performance photonics. Most importantly, the fabrication only involves a standard, silicon-compatible, reactive ion etching step and leaves the LiNbO<sub>3</sub> intact, hence its compatibility with standard foundry processes. As a proof-of-principle, we fabricated waveguides and ring resonators on the developed a-SiC/LN platform and achieved intrinsic quality factors higher than  $1.06 \times 10^5$  and a resonance electro-optic tunability of 3.4 pm/V with a 3 mm tuning length. We showcase the possibility of dense integration by fabricating and testing ring resonators with a 40 μm radius without a noticeable loss penalty. Our platform offers a CMOS-compatible and scalable approach for the implementation of future fast electro-optic modulators and reconfigurable photonic circuits, as well as nonlinear processes that can benefit from involving both second- and third-order nonlinearities.

© 2025 Author(s). <https://doi.org/10.1063/5.0228408>

## I. INTRODUCTION

Lithium niobate (LiNbO<sub>3</sub> or LN) is a material platform widely utilized in telecommunication as electro-optical modulators, tunable photonic integrated circuits (PICs), and a variety of other applications. Lithium niobate is known for its remarkable properties, such as a broad transparency window,<sup>1,2</sup> a low loss,<sup>3-6</sup> a high second order nonlinearity coefficient,<sup>7-10</sup> a strong Pockels effect,<sup>11-13</sup> and good physical and chemical stability.<sup>14</sup> The platform has been employed in studies in optical communications,<sup>13,15-17</sup> microwave photonics,<sup>13,18</sup> and quantum computing.<sup>19-23</sup>

To fabricate LiNbO<sub>3</sub> PICs, approaches ranging from titanium in-diffusion,<sup>24,25</sup> proton exchange,<sup>26,27</sup> direct etching,<sup>5,28,29</sup> dielectric

rib-loading circuits,<sup>30,31</sup> wafer bonding,<sup>17,32</sup> and plasmonic waveguides<sup>33</sup> have been successfully demonstrated. The first two methods use bulk LN substrate and locally alter the refractive index in a certain volume to create a small index contrast with respect to the substrate and cladding. These methods can only create weak confinement and hence result in high bending losses, and, moreover, they have contamination issues, and the fabrication processes are time consuming.<sup>34</sup> In contrast, direct etched waveguides and rib-loading circuits based on thin film lithium niobate (TFLN) substrates can overcome these challenges. With the smart-cut technology, a LiNbO<sub>3</sub> thin film with a thickness of less than 1 μm can be transferred and bonded to an acceptor substrate, which forms the lithium niobate on an insulator substrate.<sup>35,36</sup> Dry

etching methods such as reactive ion etching or argon milling etching are commonly chosen to define the PICs on these TFLN films<sup>29,36,37</sup> and have already proven high quality and ultralow loss photonic devices.<sup>6</sup> However, direct LN etching also has a number of disadvantages: low selectivity between LN and etching masks, a non-vertical sidewall angle (typically around 60°), and re-deposition of etching by-products such as lithium fluoride (LiF), which is difficult to remove at low temperature, are examples of these issues. In addition, and crucially, the etching of LN is not compatible with complementary metal–oxide–semiconductor (CMOS) fabrication lines, since the etching by-products and lithium out-diffusion are considered as contamination.<sup>25,38</sup> All of these problems are limiting the possibilities in design and hampering the way toward large scale fabrication and mass production.

Hybrid integration of rib-loading waveguides with TFLN offers another feasible path to fabricate compact, low loss, and scalable PICs.<sup>31</sup> The integration can be realized using two different schemes, namely, transferring/bonding a pre-fabricated PIC wafer/chip onto a TFLN substrate or deposition/sputtering of a thin film directly on the TFLN substrate followed by the fabrication of the rib-loading waveguides on this layer. Regarding the former, various techniques are used to fabricate the heterogeneous platforms.<sup>17,32,39–42</sup> Challenges from the transfer bonding process include layer-to-layer misalignment, thermal stress mismatch, and surface non-uniformity and roughness.<sup>43–46</sup> To circumvent the mentioned disadvantages associated with transfer bonding, delicate and costly procedures such as ion-slicing and multiple rounds of chemical mechanical polishing (CMP) have been utilized, which adds further complexities and limitations. In contrast, the deposition and etching scheme is a comparatively more stable and convenient approach. Various materials, such as amorphous silicon (a-Si), silicon nitride (SiN), tantalum pentoxide (Ta<sub>2</sub>O<sub>5</sub>), and titanium dioxide (TiO<sub>2</sub>), have been deposited/sputtered on TFLN, and heterogeneous PIC devices on these platforms have been demonstrated.<sup>30,47–58</sup> Bound states in continuum (BICs) photonic waveguides, which have been exploited to provide low propagation loss and overcome the challenges in single-crystal materials etching, are used for the heterogeneous integration with LN.<sup>59–61</sup> Among them, a-Si on the TFLN platform offers the merits of a small footprint and large thermal-optics tunability but suffers from a narrow bandgap, high optical loss, and weak mode interaction with LiNbO<sub>3</sub>, while silicon nitride on TFLN possesses a lower index contrast and, therefore, requires a larger waveguide bending radius to prevent bending losses. For other counterparts, in addition to similar issues as a-Si and SiN, they also suffer from incompatibility with CMOS foundries or immature fabrication processes.

Amorphous silicon carbide (a-SiC) has recently emerged as a promising option for PICs thanks to its strong optical confinement, wide transparent window, high thermo-optical coefficient, low loss, and high Kerr nonlinear coefficient.<sup>62–71</sup> Compared to the different polytypes of crystalline silicon carbide used in photonics (3C–SiC, 4H–SiC, or 6H–SiC), amorphous silicon carbide material properties can be easily tuned by changing deposition parameters, allowing precise film thickness control and offering a ten times higher Kerr nonlinear coefficient,<sup>66–68,70</sup> providing broader possibilities in the field of nonlinear optics. It has been proposed that a-SiC is a more enticing candidate compared to SiN for efficient integration of quantum dots in quantum photonics circuits.<sup>71</sup> Notably,

a-SiC can be deposited at low temperature ( $\leq 150^\circ\text{C}$ ) using inductively coupled plasma chemical vapor deposition (ICPCVD) without sacrificing the film quality, which indicates that lift-off of a-SiC films and monolithic integration of devices with different thicknesses and on different platforms are possible.<sup>62,69,72,73</sup> Essentially, the a-SiC rib-loading scheme can fulfill all the merits expected for the heterogeneous integration with TFLN, which enhances a multitude of possible applications, including compact and ultra-fast optical modulators, high density and low loss passive PICs, second order nonlinearity and Kerr nonlinearity, and deterministic integration of single photon sources for quantum photonic applications.

For the first time, an a-SiC/TFLN (or a-SiC/LN) heterogeneous photonic integration platform is proposed and investigated in this paper. Based on an optimized ICPCVD a-SiC on the TFLN fabrication process, we designed, fabricated, and characterized on-chip photonic devices and analyzed their performance. Our results demonstrate the high potential of the proposed platform in future PIC applications.

## II. METHODS AND RESULTS

### A. Fabrication

We fabricated the a-SiC rib-loading PICs on the LNOI substrates (NanoLN), which consists of 500 nm TFLN on a 2  $\mu\text{m}$  buried SiO<sub>2</sub> layer on a 300  $\mu\text{m}$  Si substrate. As shown in Fig. 1(a), 260 nm a-SiC deposition was done via ICPCVD in Oxford PlasmaPro 100 with mixed precursors of silane (SiH<sub>4</sub>) and methane (CH<sub>4</sub>) at a table temperature of 150 °C. Argon (Ar) flow was chosen as the deposition environment. The chamber pressure is set to 2 mTorr.<sup>62</sup> It is known that high temperature processes can potentially cause problems, such as unwanted diffusion, non-releasable thermal stress, or thermal expansion mismatch, which renders the fabrication process CMOS incompatible. The low-temperature deposited ICPCVD a-SiC film mitigates these challenges and allows the monolithic integration of PICs with different thicknesses on TFLN.<sup>62</sup> After a-SiC deposition, ellipsometry measurements were performed (Woollam M-2000 spectroscopic ellipsometer) to get the refractive index of a-SiC. The real and imaginary refractive index ( $n$  and  $k$ ) results are shown in Fig. 1(c). Around 1550 nm, the wavelength of interest in this work, the complex refractive index is found to be  $2.73 + i8.4 \times 10^{-5}$  (fitted by the B-spline expanded Cauchy model with Cody–Lorentz oscillators). To determine the surface roughness, which places a significant impact on the optical waveguide loss, we conducted an atomic force microscopy (AFM) measurement in a  $4 \times 4 \mu\text{m}^2$  region on the top surface of an a-SiC film [shown in Fig. 1(b)]. We obtained a root-mean-square (rms) value of  $(0.45 \pm 0.06)$  nm, indicating good deposition quality and surface flatness.

Fabrication flow for electro-optically tunable devices is shown in Fig. 1(d). To fabricate the PIC waveguides, electron beam lithography (EBL) resist (CSAR 62) was spin-coated and baked at 160 °C for 2 min. The rib-loading PIC pattern was defined on the resist layer by EBL exposure (Raith 100-kV EBPG-5200), and after development, it was transferred to the a-SiC layer by reactive-ion etching (RIE, Sentech Etchlab 200) using a gas mixture of SF<sub>6</sub> and O<sub>2</sub>. The etching time was carefully controlled to prevent over-etching. The electrodes for electro-optics devices are fabricated by a standard lift-off process. Based on the electrode patterns pre-defined by another

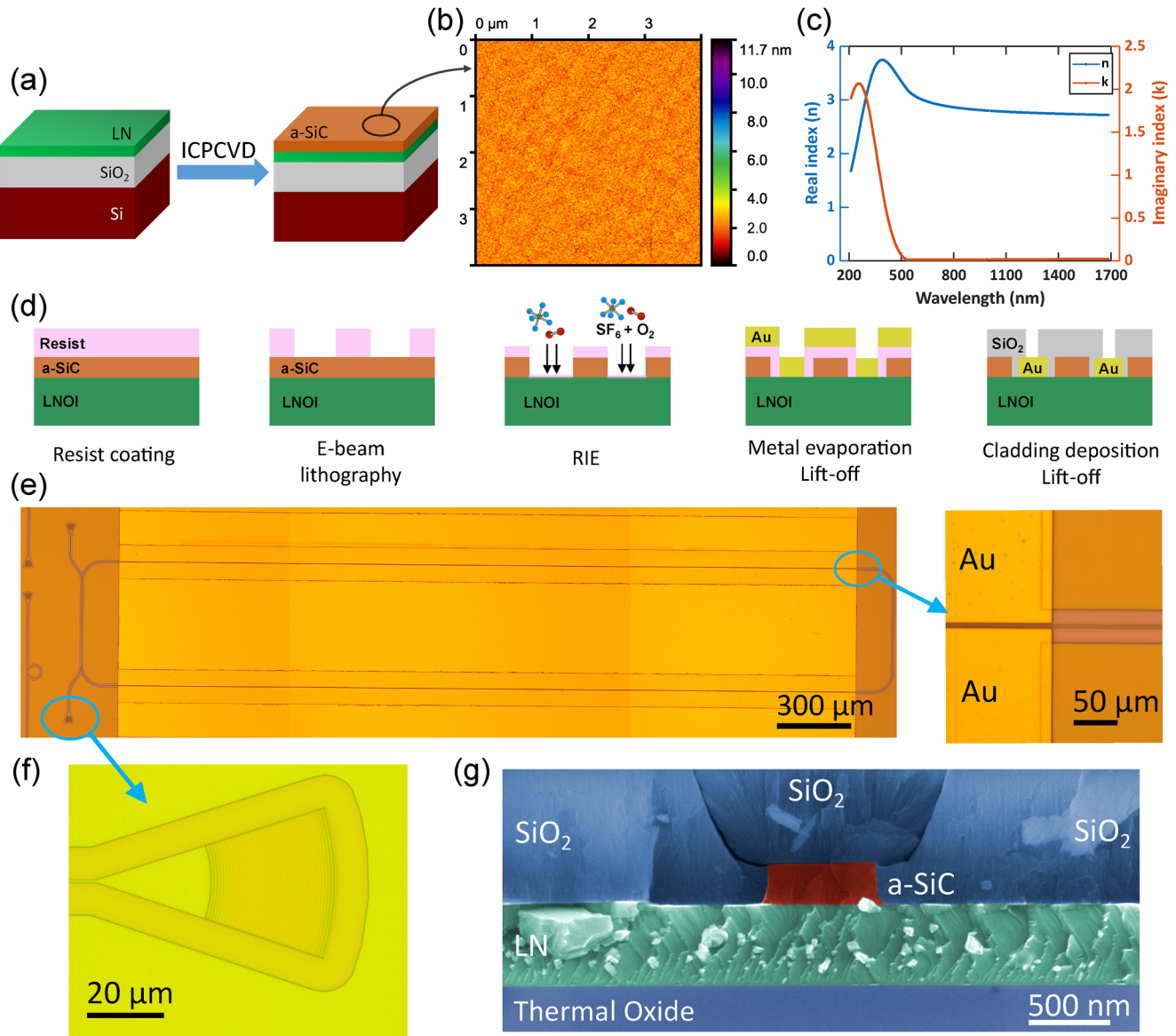


**FIG. 1.** (a) a-SiC thin film deposition on LNOI substrate. (b) AFM measurement results on an a-SiC surface. (c) Real and imaginary refractive index ( $n$  and  $k$ ) of the a-SiC film. (d) Fabrication flow of electro-optical tunable a-SiC/TFLN devices. (e) Optical microscopy image (stitched) of a fabricated racetrack ring resonator, with the inset: region of the waveguide between two Au electrodes. (f) Optical microscopy image of the grating coupler. (g) False colored scanning electron microscope (SEM) image of an a-SiC/LN waveguide cross section. a-SiC is colored in red, LN in green, while the top (ICPCVD SiO<sub>2</sub>) and bottom oxide (thermal oxide) layers are in blue.

EBL step, the electrodes are fabricated by an electron beam evaporation of 10 nm chromium (Cr) and 450 nm gold (Au), followed by a lift-off process in resist stripper (PRS-3000). Since the ICPCVD SiO<sub>2</sub> can also be deposited at low temperature (150 °C), it is compatible with the standard lift-off process; the same EBL/lift-off procedure is employed to fabricate the SiO<sub>2</sub> cladding. The thickness of the cladding is larger than 1.1 μm. The SiO<sub>2</sub> cladding covers all the optical devices but leaves the Au electrodes exposed for the convenience of wire-bonding. Following each EBL exposure step, the resist was

developed and reflowed at 130 °C for 1 min after development in order to enhance the etching aspect-ratio and reduce the sidewall roughness. It is essential to further clean the resist residuals using oxygen plasma after every chemical lift-off process to maintain the surface roughness given by ICPCVD deposition and reduce optical scattering brought by remaining particles on the surface. A stitched optical microscopy image of fabricated devices is shown in Fig. 1(e), with an inset zooming in on the region of the waveguide sandwiched between the Au electrodes. An optical microscopy image of

the apodized grating couplers, which are systematically discussed in the [supplementary material](#), is presented in Fig. 1(f). The sample is cleaved, and the cross section of a passive a-SiC/LN waveguide is inspected under a scanning electron microscope (SEM). In Fig. 1(g), a false colored SEM picture illustrates the cross section profile of the a-SiC/LN waveguide. It was found out that the low-temperature ICPCVD SiO<sub>2</sub> deposition is not fully conformal, leading to air voids, which is known as the key-hole effect,<sup>74</sup> and can be observed around the top corners of the a-SiC waveguide.

### B. Design and simulation

In the heterogeneous a-SiC/TFLN platform, optical modes are confined and propagated around the rib-loading a-SiC waveguides in a way that only fundamental TE/TM modes are supported, and the mode overlapping fraction with the two materials can be engineered by altering the waveguide width. As illustrated in Figs. 2(a)–2(e), the racetrack ring resonator consists of standard

waveguides (width  $w_1 = 800$  nm and height  $h = 260$  nm), adiabatic tapers, and narrow waveguides (width  $w_2 = 400$  nm and height  $h = 260$  nm). Here, we define the mode overlapping fraction in the LN layer as  $\Gamma_{LN}$ , denoting the effective percentage of mode intensity distribution and interaction with the material LN. In the standard waveguides, optical modes are relatively strongly confined by the a-SiC waveguides, and the mode overlapping fractions of the fundamental modes are  $\Gamma_{LN-TE} = 33.65\%$  and  $\Gamma_{LN-TM} = 57.04\%$ , as shown in Figs. 2(b) and 2(c). Correspondingly, the confinement becomes weaker when the waveguide width is tapered down, which results in  $\Gamma_{LN-TE} = 66.03\%$  and  $\Gamma_{LN-TM} = 68.11\%$ , respectively [shown in Figs. 2(d) and 2(e)]. In both cases, the waveguide’s dimensions are designed to ensure that only fundamental TE and TM modes are supported. The standard waveguides are used for propagation and sharp bendings, utilizing the strong confinement property, while the narrow waveguides can be leveraged to strengthen the interaction between optical modes and LN material to enhance the EO tuning efficiency. The longer arms of the racetrack ring, marked

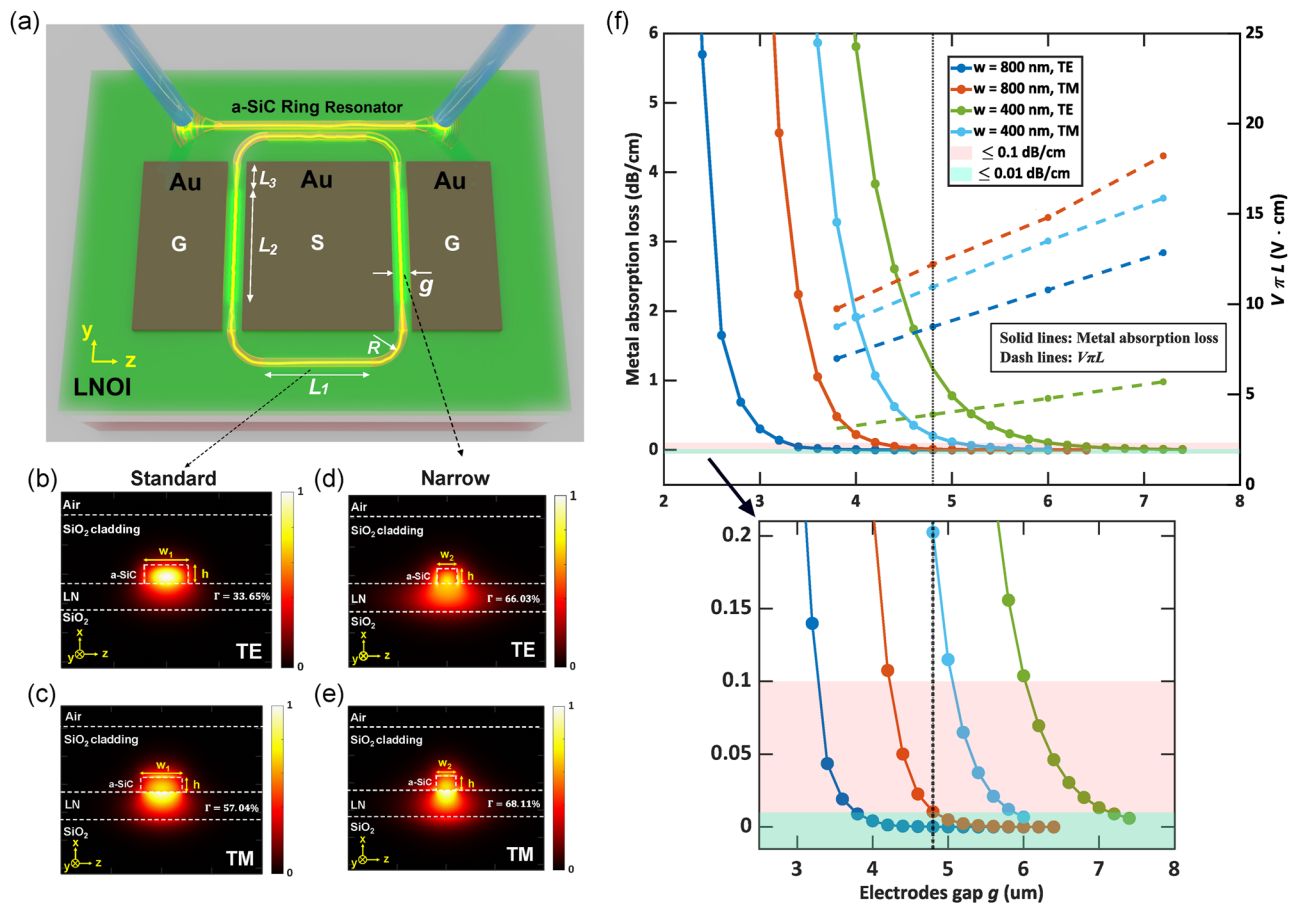


**FIG. 2.** (a) Schematic of the electro-optical tunable racetrack ring resonator. Mode distribution and mode-LN overlapping fraction of fundamental (b) TE and (c) TM modes in standard waveguides ( $w = 800$  nm). (d) TE and (e) TM modes distribution with overlapping fraction in tapered down waveguides (narrow waveguides,  $w = 400$  nm). (f) Metal absorption loss (in solid lines and left-Y axis) and half-wave voltage-length product (in dashed lines and right-Y axis) with respect to electrodes gap  $g$  change for different waveguide widths and polarizations. The areas of  $\leq 0.1$  and  $\leq 0.01$  dB/cm are shadowed by pink and cyan, respectively. The zoom figure at the bottom is a magnification of the low absorption loss region.

in Fig. 2(a) with  $L_2 = 3000 \mu\text{m}$ , are aligned perpendicular to the LN crystal z-axis [coordinate system marked at the left-bottom corners in Figs. 2(b)–2(e)] to excite the Pockels effect with the largest EO coefficient  $r_{33} = 30.9 \text{ pm/V}$ .<sup>38</sup> The mode distributions and overlapping fractions are simulated by a finite difference eigenmode solver (MODE Solutions, Ansys Lumerical) based on the material properties mentioned in Sec. II A, taking the extraordinary and ordinary refractive index of LN as  $n_e = 2.13$  and  $n_o = 2.21$  around  $1550 \text{ nm}^2$ .<sup>25</sup> The LN crystal coordinate system is marked in the figures at the left-bottom corner. Mesh grid size is chosen close to the lithography resolution, and a convergence test is performed with perfect matching layer (PML) boundary conditions. Adiabatic tapers with a length of  $L_3 = 100 \mu\text{m}$  are adopted to convert the propagation modes between the standard and narrow waveguides without extra losses.<sup>75,76</sup> The gap between the ring and bus waveguides is set to  $400 \text{ nm}$ ; together with the coupling length (shorter arm)  $L_1 = 500 \mu\text{m}$ , the racetrack ring resonator is brought to a nearly critical coupling regime. At both ends of the bus waveguide, there are two apodized grating couplers (GCs) enabling efficient in-and-out fiber coupling. These grating couplers are designed and optimized to provide wide bandwidth ( $>40 \text{ nm}$ ) and have  $\sim 6.25 \text{ dB}$  coupling loss per fiber-grating connection. The details of the design and characterization of the GCs are discussed in the supplementary material.

For EO tuning, we use a ground–signal–ground (G–S–G) electrode configuration to minimize the tuning length and device footprint, as depicted in Fig. 2(a). In order to optimize the tuning efficiency and metal absorption loss, the Charge Transport (CHARGE, Ansys Lumerical) and Finite Element EigenMode (FEEM, Ansys Lumerical) simulations are implemented. Except for the mentioned waveguide geometry, the gap  $g$  between the ground and signal is another vital variable that influences the EO tuning performance. There is an inevitable trade-off between high EO tuning efficiency (smaller  $g$ ) and low propagation loss (larger  $g$ ), which suggests that a balanced point of  $g$  needs to be engineered. Discarding waveguide material absorption and sidewall roughness (scattering losses), which are not correlated with the electrode gap  $g$ , the impact of metal absorption losses is considered when choosing the value of  $g$ . In the plane where the extraordinary  $\text{LiNbO}_3$  crystal axis is parallel aligned to the applied electric field  $E$  (this work focuses on this situation mainly), the EO tuning efficiency can be evaluated by the half-wave voltage–length product  $V_\pi \cdot L$  as

$$V_\pi \cdot L = \frac{\lambda d_{\text{eff}}}{2n_e^3 r_{33}},$$

where  $d_{\text{eff}}$  is the effective distance between the anode and cathode given the effective electric field  $E_{\text{eff}} = V/d_{\text{eff}}$

$$= \frac{V \cdot \int |E_{x,\text{optical}}|^2 dS}{\int_{\text{LN}} |E_{x,\text{optical}}|^2 \cdot E_{z,\text{electric}} dS},$$

For both TE and TM modes, the metal absorption losses and half-wave voltage–length products of the standard and narrow waveguides are simulated. As shown in Fig. 2(f), the metal absorption losses in solid lines are decreasing along with the increment of the gap  $g$ , while the half-wave voltage–length products represented in dashed lines show the opposite trend. Clear polarization dependence can be seen from the results, due to the difference in refractive indices and EO coefficients along the ordinary and extraordinary axes ( $r_{33} = 30.9 \text{ pm/V}$  and  $r_{13} = 9.6 \text{ pm/V}$ ). The narrowed waveguide

structure has a larger fraction of the optical mode concentrated in the LN layer, resulting in larger EO-tuning efficiency but also suffering more from metal absorption. The areas where the metal absorption loss is no larger than  $0.1$  and  $0.01 \text{ dB/cm}$  are marked with pink and cyan, respectively. At a studied wavelength of  $1550 \text{ nm}$ , the electrode gap  $g \geq 4.8 \mu\text{m}$  is considered to introduce negligible losses for both TE and TM modes in the standard waveguides ( $\leq 0.01 \text{ dB/cm}$ ), corresponding to the estimated half-wave voltage–length products of  $8.8$  and  $12.3 \text{ V cm}$ . For the TE mode in the narrow waveguides, the metal absorption loss is negligible when  $g = 6.0 \mu\text{m}$ , corresponding to an efficiency of  $4.7 \text{ V cm}$ . The TM mode in the narrow waveguides does not suffer from extra absorption when  $g = 7.2 \mu\text{m}$  and has an EO-tuning efficiency of  $15.9 \text{ V cm}$ . Other values of waveguide width and electrode gap are considered, and the corresponding metal absorption, half-wave voltage–length product, and effective index change when applying  $0\text{--}20 \text{ V DC}$  voltages are simulated and presented in Fig. S6 of the supplementary material. After an overall comparison, the preferably balanced combination of waveguide width ( $w = 800 \text{ nm}$ ) and electrode gap ( $g = 4.8 \mu\text{m}$ ) indicated by the black dashed line in Fig. 2(f) is chosen to experimentally show the principle of the passive and active devices on the a-SiC/LN platform. To push for higher electro-optics tuning efficiency, the configuration of tapering down waveguides and  $g = 6.0 \mu\text{m}$  can be used for which  $4.7 \text{ V cm}$  EO-tuning efficiency is expected. Note that in the latter case (tapered waveguide), only the TE mode maintains the intrinsic loss. Tapering down the waveguides to narrower widths will possibly reduce the scattering loss, since the large proportion of the optical mode will be located in the not etched LN, resulting in less absorption from a-SiC and less scattering caused by the sidewall roughness.<sup>30</sup>

### C. Characterization of passive optical devices

Thin film quality and waveguide propagation loss were characterized using ring resonators with intrinsic quality factor  $Q_i$ ,<sup>62</sup> which is defined as

$$Q_i = \frac{2Q_L}{1 + \sqrt{T}} = \frac{2\lambda_0}{FWHM(1 + \sqrt{T})},$$

where  $Q_L$  is the loaded quality factor,  $\lambda_0$  is the resonance wavelength,  $FWHM$  represents the full-width half-maximum of the resonance dip, and  $T$  is the on-resonance transmission. To extract the propagation loss from the intrinsic quality factor,<sup>62</sup> we calculate the loss  $\alpha$  as

$$\alpha \text{ (dB/m)} = 4.3429 \cdot \alpha \text{ (m}^{-1}\text{)} = 4.3429 \cdot \left( \frac{2\pi n_g}{Q_i \lambda_0} \right),$$

where the group index  $n_g$  is derived from the free spectral range (FSR) of the optical cavity,

$$n_g = \frac{\lambda_0^2}{L_{\text{total}} \cdot \text{FSR}} = \frac{\lambda_0^2}{2(\pi R + L_2 + L_1) \cdot \text{FSR}},$$

in which  $L_{\text{Total}}$  represents the total length of the ring. The FSR can be obtained from the resonance spectra shown in Figs. 3(a) and 3(b). In comparison to the simulation results mentioned in Sec. II B, for a ring consisting of normal waveguides ( $260 \times 800 \text{ nm}^2$ ), the simulated group indices for TE and TM modes are

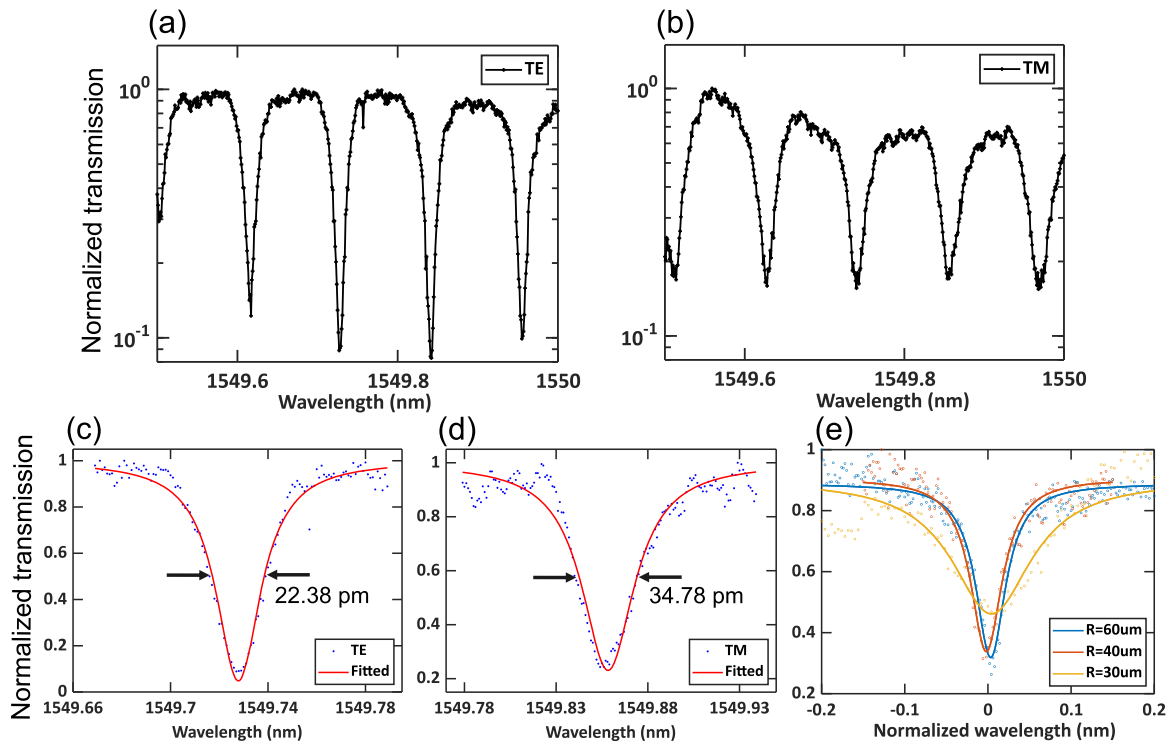


**FIG. 3.** Characterization of optical properties in the standard waveguide ring resonators: Normalized transmission spectra (dots, log scale) of (a) fundamental TE mode and (b) TM mode. Lorentz fitted resonance dips of (c) TE mode with  $FWHM = 22.38$  pm and (d) TM mode with  $FWHM = 34.78$  pm. (e) Lorentz fitted resonance dips of ring resonators with different bending radii.

$n_{gTE} = 2.738$  and  $n_{gTM} = 2.614$  at 1550 nm, corresponding to  $FSR$  of 113 and 118 pm, respectively, which are in good agreement with the experimental results. Single resonance peaks acquired from the TE and TM spectra are fitted by the Lorentzian function [Figs. 3(c) and 3(d)], showing a  $FWHM$  of 22.38 pm for the TE mode and 34.78 pm for the TM mode, respectively. The calculated intrinsic quality factor for TE mode is 106 673, denoting a propagation loss of 4.48 dB/cm.

Ring resonators with different bending radii are fabricated and measured to analyze the influence of bending loss. The Lorentzian fitting of the resonance dips from different rings is brought together in Fig. 2(f) for comparison, in which one can see when decreasing the bending radius, the  $FWHM$  does not change until  $R = 40 \mu\text{m}$ , while the  $FWHM$  becomes much wider from  $R = 40 \mu\text{m}$  to  $R = 30 \mu\text{m}$ . In particular, the change of bending radius  $R$  from 60 to 40  $\mu\text{m}$  brings a  $FWHM$  change of  $\sim 3$  pm, while reducing the  $R$  to 30  $\mu\text{m}$  results in a  $FWHM$  increment of  $\sim 72$  pm. It is inferred that the intrinsic quality factor has no noticeable change related to the change of bending radius from 60 to 40  $\mu\text{m}$ , and the bending loss is negligible for  $R \geq 40 \mu\text{m}$ . This enables denser integration compared with SiN rib-loading waveguides. Nevertheless, in the following context, we discuss electro-optics tuning; the bending radius of racetrack ring resonators is kept to 120  $\mu\text{m}$ , leaving more space for wire-bonding and minimizing the impact of bending losses.

#### D. Characterization of EO tunability

The electro-optics response of the a-SiC/LN platform is characterized and analyzed. Figure 4(a) depicts the characterization setup; starting from a tunable laser (Photonics TUNICS-PRI 3642 HE 15), the light passes through a paddle polarization controller and a free-space polarizer (Thorlabs FBR-LPNIR). The free-space polarizer is used to select specific polarizations, while the paddle polarization controller aligns the input light to the selected polarization. The polarized light is then coupled by a polarization maintaining fiber into the a-SiC/LN device by the on-chip apodized grating coupler. The output light is coupled out from another apodized grating coupler and collected by an optical powermeter (Newport 818-NR). To measure the electro-optics response, the sample is mounted on a printed circuit board (PCB), as shown in Fig. 4(b). Afterward, the on-chip Au electrodes are wire-bonded to the PCB [Fig. 4(c)]. A programmable voltage supply (RIGOL model DP832A) is used to generate DC voltage signals, of which the ground and output ports are connected to the pads on the PCB by probes.

On the proposed heterogeneous a-SiC on the TFLN platform, the direct current (DC) driven Pockels effect is investigated to quantify the platform's tunability performance. As shown in the diagram in Fig. 2(a), the racetrack ring resonator with Au electrodes is in a push-pull configuration, with normal waveguide dimensions ( $260 \times 800 \text{ nm}^2$ ) and gap  $g = 4.8 \mu\text{m}$ . Fundamental TE and TM modes are excited and characterized when voltage sweeping is



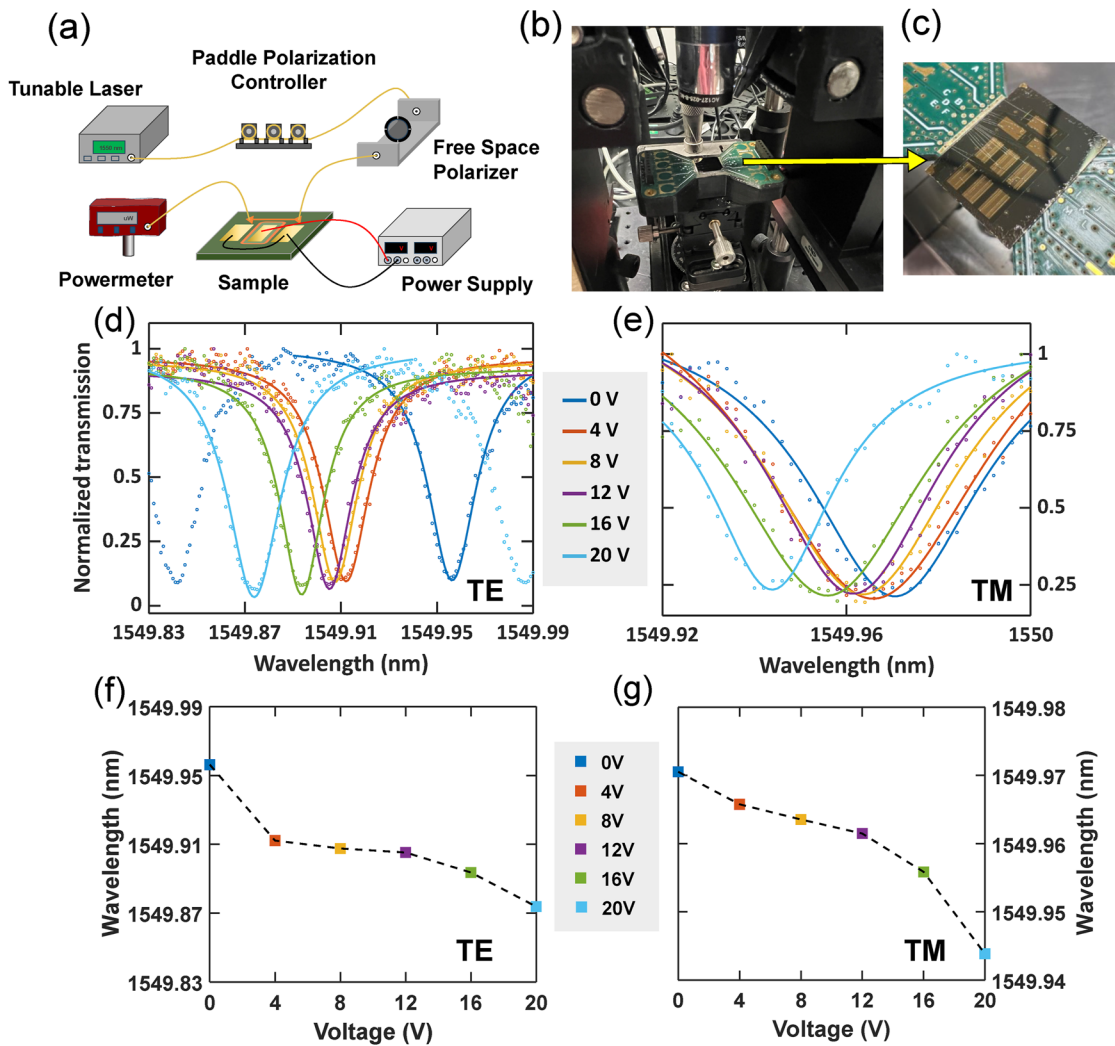


**FIG. 4.** (a) Schematic diagram and (b) image of the characterization setup. (c) a-SiC/TFLN sample mounted and wire-bonded onto the PCB that is connected to the power supply. Normalized transmission spectra of (d) TE mode and (e) TM mode propagated in the ring resonator when DC voltages applied (dots for raw data and solid lines for Lorentzian fittings). Resonance wavelength position with respect to DC voltage change of (f) TE mode and (g) TM mode, the raw data (square dots) are connected by dashed lines as guides for the eyes.

performed on the Au electrodes, shown in Figs. 4(d) and 4(e). The center wavelengths of the resonance dips are extracted and plotted in Figs. 4(f) and 4(g). While a linear EO tuning is expected, in Figs. 4(f) and 4(g) it is clear that certain data-points deviate from the linear behavior. These deviations can be ascribed to the DC bias drift of the LiNbO<sub>3</sub> crystal and the laser positioning error in wavelength. The bias point drift behavior is known in the literature.<sup>77–80</sup> The estimated resonance tunability of 3.4 and 1.2 pm/V can be obtained for TE mode and TM mode, respectively. We calculated the approximate half-wave voltage–length products and obtained 9.79 V cm for the TE mode and 27.5 V cm for the TM mode. The difference between the simulation results and experimental results is believed

to stem from the misalignment between the racetrack’s longer arms and the LN crystal axis.

### III. DISCUSSION AND CONCLUSION

In conclusion, we proposed the a-SiC/TFLN (or a-SiC/LN) heterogeneous photonic integrated platform, and it has been realized by a CMOS compatible fabrication process at a temperature lower than 165 °C. Optical ring resonators are characterized, and an intrinsic quality factor of  $1.06 \times 10^5$  is measured. The Pockels effect is evaluated on this platform by applying an electric field perpendicular to the mode propagation; consequently, 3.4 pm/V

**TABLE I.** Comparison of performance and fabrication of different rib-loading materials on lithium niobate heterogeneous/hybrid photonic integrated platforms.

Platform	Bending radius ( $\mu\text{m}$ )	$Q_i$ and (or) loss <sup>a</sup>	LN etching	Wafer bonding <sup>b</sup>	CMP	Max. Temp. ( $^{\circ}\text{C}$ )	DC-EO $V_{\pi}L$ (V cm)	References
3C-SiC/LNOI	35	$2.2 \times 10^4$ , 19.2 dB/cm	No	Yes	Yes	100	3.15	39
aSiC/LNOI	40	$1.1 \times 10^5$ , 4.48 dB/cm	No	No	No	160	9.79	This work.
Si/LNOI	15	$2.14 \times 10^4$ , 32.87 dB/cm <sup>c</sup>	No	Yes	No	1000	9.1	40
a-Si/LNOI	15	42 dB/cm	No	No	Yes	350	...	48
SiN/LNOI	300	$1.3 \times 10^5$	No	No	No	300	5.1	50
SiN/LNOI	225	$4.5 \times 10^6$ , 0.085 dB/cm	Yes	Yes	Yes	1200	8.8	32
BICs/LNOI	$\sim 70$	1.5 dB/cm	No	No	No	...	$\sim 16$	61

<sup>a</sup>For x-cut LN and TE-polarized propagation mode.

<sup>b</sup>Wafer bonding contains the processes of adhesive layer preparing, bonding, and handle removal; sometimes annealing is also incorporated.

<sup>c</sup>Calculated from the reported data.

resonance tunability is achieved in the ring resonator. Table I listed the information on different rib-loading waveguides on lithium niobate heterogeneous/hybrid photonic platforms, comparing the details in performance and fabrication complexity. The applications of this a-SiC/LN platform can be extended to high-speed optical communications, programmable photonics, optical computing, nonlinear optics, and quantum optics. By narrowing the waveguide width, lower propagation loss and higher EO-tuning efficiency with a half-wave voltage-length product of 4.7 V cm can possibly be achieved for the TE mode. In the narrow waveguides, the propagation loss is also expected to decrease due to a large proportion of the optical mode located in the not etched LN, regarding less absorption from a-SiC and less scattering loss from the sidewall roughness. The key-hole effect observed in the oxide cladding is considered to be one of the reasons that reduces the ring quality factors, and hence the loss performance can be potentially improved by applying more conformal claddings, such as Tetraethyl Orthosilicate (TEOS), or optimizing the conformality of the ICPCVD  $\text{SiO}_2$  deposition process. The optical loss may still be further improved by optimizing the a-SiC deposition and etching on LN and adding an annealing step.<sup>81</sup> The waveguide dimensions (thickness and width) can be further engineered to significantly reduce the half-wave voltage-length product (for 260 nm narrow waveguides,  $V_{\pi}L$  is estimated to be 4.7 V cm; reducing a-SiC thickness can possibly push it to even lower values). Feed-back loops and active corrections can be implemented to counter the bias point drift induced by long time applied DC-voltage. In principle, the same heterogeneous integration can be applied on bulk lithium niobate substrates as well, utilizing higher nonlinear coefficients and a stronger Pockels effect compared to thin film  $\text{LiNbO}_3$ . Furthermore, the methods developed here, particularly low-temperature ICPCVD a-SiC, constitute a promising route for heterogeneous integration with other substrates, such as diamond, yttrium iron garnet (YIG), barium borate (BBO), lithium tantalate ( $\text{LiTaO}_3$ ), yttrium aluminum garnet (YAG), barium titanate (BTO), and lead zirconate titanate (PZT). Therefore, with further development and optimization, the demonstrated platform holds great potential for future heat-free, tunable, integrated photonics and represents a fundamental building block for second- and third-order non-linearities in quantum communication and optical quantum computing.

## SUPPLEMENTARY MATERIAL

More information about the fabrication, grating couplers used for in-and-out coupling, and electrodes for electro-optics measurement can be found in the [supplementary material](#).

## ACKNOWLEDGMENTS

The authors acknowledge the valuable comments and suggestions from Sylvania Pereira. Z.L. acknowledges the China Scholarship Council (CSC, Grant No. 202206460012). N.S. and I.E.Z. acknowledge the funding from the NWO OTP COMB-O project (Project No. 18757). I.E.Z. acknowledges the funding from the European Union's Horizon Europe research and innovation program under Grant Agreement Nos. 101098717 (RESPITE project) and 101099291 (fastMOT project).

## AUTHOR DECLARATIONS

### Conflict of Interest

The authors have no conflicts to disclose.

## Author Contributions

**Zizheng Li:** Conceptualization (equal); Data curation (equal); Formal analysis (equal); Investigation (equal); Methodology (equal); Project administration (equal); Resources (equal); Software (equal); Supervision (equal); Validation (equal); Visualization (equal); Writing – original draft (equal); Writing – review & editing (equal). **Naresh Sharma:** Conceptualization (equal); Data curation (equal); Formal analysis (equal); Investigation (equal); Methodology (equal); Project administration (equal); Resources (equal); Software (equal); Supervision (equal); Validation (equal); Visualization (equal); Writing – original draft (equal); Writing – review & editing (equal). **Bruno Lopez-Rodriguez:** Conceptualization (equal); Formal analysis (equal); Investigation (equal); Methodology (equal); Resources (equal); Validation (equal); Writing – original draft (equal); Writing – review & editing (equal). **Roald van der Kolk:** Data curation (equal); Resources (equal); Software (equal); Validation (equal); Visualization (equal); Writing – review & editing (equal). **Thomas**

**Scholte:** Investigation (equal); Methodology (equal); Resources (equal); Software (equal); Validation (equal); Writing – review & editing (equal). **Hugo Voncken:** Data curation (equal); Investigation (equal); Software (equal); Validation (equal). **Jasper van der Boom:** Software (equal); Visualization (equal). **Simon Gröblacher:** Conceptualization (equal); Supervision (equal); Writing – original draft (equal); Writing – review & editing (equal). **Iman Esmail Zadeh:** Conceptualization (equal); Formal analysis (equal); Funding acquisition (equal); Investigation (equal); Methodology (equal); Project administration (equal); Resources (equal); Software (equal); Supervision (equal); Validation (equal); Visualization (equal); Writing – original draft (equal); Writing – review & editing (equal).

## DATA AVAILABILITY

The data that support the findings of this study are available from the corresponding author upon reasonable request.

## REFERENCES

- A. R. Zanatta, “The optical bandgap of lithium niobate ( $\text{LiNbO}_3$ ) and its dependence with temperature,” *Results Phys.* **39**, 105736 (2022).
- H. Han, L. Cai, and H. Hu, “Optical and structural properties of single-crystal lithium niobate thin film,” *Opt. Mater.* **42**, 47–51 (2015).
- R. Wu, J. Zhang, N. Yao, W. Fang, L. Qiao, Z. Chai, J. Lin, and Y. Cheng, “Lithium niobate micro-disk resonators of quality factors above  $10^7$ ,” *Opt. Lett.* **43**, 4116–4119 (2018).
- X. Zhu, Y. Hu, S. Lu, H. K. Warner, X. Li, Y. Song, L. Magalhães, A. Shams-Ansari, A. Cordaro, N. Sinclair *et al.*, “Twenty-nine million intrinsic q-factor monolithic microresonators on thin-film lithium niobate,” *Photonics Res.* **12**, A63–A68 (2024).
- R. Zhuang, J. He, Y. Qi, and Y. Li, “High-Q thin-film lithium niobate microrings fabricated with wet etching,” *Adv. Mater.* **35**, 2208113 (2023).
- B. Desiatov, A. Shams-Ansari, M. Zhang, C. Wang, and M. Lončar, “Ultra-low-loss integrated visible photonics using thin-film lithium niobate,” *Optica* **6**, 380–384 (2019).
- J. Ma, J. Chen, M. Ren, W. Wu, W. Cai, and J. Xu, “Second-harmonic generation and its nonlinear depolarization from lithium niobate thin films,” *Opt. Lett.* **45**, 145–148 (2020).
- S. Yuan, Y. Wu, Z. Dang, C. Zeng, X. Qi, G. Guo, X. Ren, and J. Xia, “Strongly enhanced second harmonic generation in a thin film lithium niobate heterostructure cavity,” *Phys. Rev. Lett.* **127**, 153901 (2021).
- P.-K. Chen, I. Briggs, C. Cui, L. Zhang, M. Shah, and L. Fan, “Adapted poling to break the nonlinear efficiency limit in nanophotonic lithium niobate waveguides,” *Nat. Nanotechnol.* **19**, 44–50 (2024).
- C. Wang, M. Zhang, M. Yu, R. Zhu, H. Hu, and M. Lončar, “Monolithic lithium niobate photonic circuits for Kerr frequency comb generation and modulation,” *Nat. Commun.* **10**, 978 (2019).
- R. Weis and T. Gaylord, “Lithium niobate: Summary of physical properties and crystal structure,” *Appl. Phys. A: Solids Surf.* **37**, 191–203 (1985).
- M. Thomaschewski and S. Bozhevolnyi, “Pockels modulation in integrated nanophotonics,” *Appl. Phys. Rev.* **9**, 021311 (2022).
- A. Boes, L. Chang, C. Langrock, M. Yu, M. Zhang, Q. Lin, M. Lončar, M. Fejer, J. Bowers, and A. Mitchell, “Lithium niobate photonics: Unlocking the electromagnetic spectrum,” *Science* **379**, eabj4396 (2023).
- Y. Kong, F. Bo, W. Wang, D. Zheng, H. Liu, G. Zhang, R. Rupp, and J. Xu, “Recent progress in lithium niobate: Optical damage, defect simulation, and on-chip devices,” *Adv. Mater.* **32**, 1806452 (2020).
- C. Wang, M. Zhang, X. Chen, M. Bertrand, A. Shams-Ansari, S. Chandrasekhar, P. Winzer, and M. Lončar, “Integrated lithium niobate electro-optic modulators operating at CMOS-compatible voltages,” *Nature* **562**, 101–104 (2018).
- M. Li, J. Ling, Y. He, U. A. Javid, S. Xue, and Q. Lin, “Lithium niobate photonic crystal electro-optic modulator,” *Nat. Commun.* **11**, 4123 (2020).
- M. He, M. Xu, Y. Ren, J. Jian, Z. Ruan, Y. Xu, S. Gao, S. Sun, X. Wen, L. Zhou *et al.*, “High-performance hybrid silicon and lithium niobate Mach-Zehnder modulators for 100 Gbit  $s^{-1}$  and beyond,” *Nat. Photonics* **13**, 359–364 (2019).
- L. Shao, M. Yu, S. Maity, N. Sinclair, L. Zheng, C. Chia, A. Shams-Ansari, C. Wang, M. Zhang, K. Lai, and M. Lončar, “Microwave-to-optical conversion using lithium niobate thin-film acoustic resonators,” *Optica* **6**, 1498–1505 (2019).
- A. Maeder, G. Finco, F. Kaufmann, A. Sabatti, J. Kellner, R. J. Chapman, and R. Grange, “On-chip tunable quantum interference in a lithium niobate-on-insulator photonic integrated circuit,” *Quantum Sci. Technol.* **9**, 035040 (2024).
- O. Alibart, V. D’Auria, M. De Micheli, F. Doutre, F. Kaiser, L. Labonté, T. Lungli, E. Picholle, and S. Tanzilli, “Quantum photonics at telecom wavelengths based on lithium niobate waveguides,” *J. Opt.* **18**, 104001 (2016).
- R. J. Chapman, S. Häusler, G. Finco, F. Kaufmann, and R. Grange, “Quantum logical controlled-not gate in a lithium niobate-on-insulator photonic quantum walk,” *Quantum Sci. Technol.* **9**, 015016 (2023).
- X. Wang, X. Jiao, B. Wang, Y. Liu, X.-P. Xie, M.-Y. Zheng, Q. Zhang, and J.-W. Pan, “Quantum frequency conversion and single-photon detection with lithium niobate nanophotonic chips,” *npj Quantum Inf.* **9**, 38 (2023).
- M. J. Weaver, P. Duivesteyn, A. C. Bernasconi, S. Scharmer, M. Lemang, T. C. v. Thiel, F. Hijazi, B. Hensen, S. Gröblacher, and R. Stockill, “An integrated microwave-to-optics interface for scalable quantum computing,” *Nat. Nanotechnol.* **19**, 166–172 (2024).
- R. Becker, “Comparison of guided-wave interferometric modulators fabricated on  $\text{LiNbO}_3$  via Ti indiffusion and proton exchange,” *Appl. Phys. Lett.* **43**, 131–133 (1983).
- G. Chen, N. Li, J. D. Ng, H.-L. Lin, Y. Zhou, Y. H. Fu, L. Y. T. Lee, Y. Yu, A.-Q. Liu, and A. J. Danner, “Advances in lithium niobate photonics: Development status and perspectives,” *Adv. Photonics* **4**, 034003 (2022).
- G. R. Paz-Pujalt, D. D. Tuschel, G. Braunstein, T. Blanton, S. T. Lee, and L. M. Salter, “Characterization of proton exchange lithium niobate waveguides,” *J. Appl. Phys.* **76**, 3981–3987 (1994).
- A. Loni, “An experimental study of proton-exchanged lithium niobate optical waveguides,” Ph.D. thesis, University of Glasgow, 1987.
- S. Y. Siew, E. J. H. Cheung, H. Liang, A. Bettiol, N. Toyoda, B. Alshehri, E. Dogheche, and A. J. Danner, “Ultra-low loss ridge waveguides on lithium niobate via argon ion milling and gas clustered ion beam smoothing,” *Opt. Express* **26**, 4421–4430 (2018).
- Z. Li, R. N. Wang, G. Lihachev, J. Zhang, Z. Tan, M. Churayev, N. Kuznetsov, A. Siddharth, M. J. Beryhi, J. Riemensberger *et al.*, “High density lithium niobate photonic integrated circuits,” *Nat. Commun.* **14**, 4856 (2023).
- X. Huang, Y. Liu, Z. Li, Z. Fan, and W. Han, “High-performance and compact integrated photonics platform based on silicon rich nitride-lithium niobate on insulator,” *APL Photonics* **6**, 116102 (2021).
- X. Han, M. Yuan, H. Xiao, G. Ren, T. G. Nguyen, A. Boes, Y. Su, A. Mitchell, and Y. Tian, “Integrated photonics on the dielectrically loaded lithium niobate on insulator platform,” *J. Opt. Soc. Am. B* **40**, D26–D37 (2023).
- M. Churayev, R. N. Wang, A. Riedhauser, V. Snigirev, T. Blésin, C. Möhl, M. H. Anderson, A. Siddharth, Y. Popoff, U. Drechsler *et al.*, “A heterogeneously integrated lithium niobate-on-silicon nitride photonic platform,” *Nat. Commun.* **14**, 3499 (2023).
- M. Thomaschewski, V. A. Zenin, C. Wolff, and S. I. Bozhevolnyi, “Plasmonic monolithic lithium niobate directional coupler switches,” *Nat. Commun.* **11**, 748 (2020).
- T. Ranganath and S. Wang, “Suppression of  $\text{Li}_2\text{O}$  out-diffusion from Ti-diffused  $\text{LiNbO}_3$  optical waveguides,” *Appl. Phys. Lett.* **30**, 376–379 (1977).
- G. Poberaj, M. Koechlin, F. Sulser, A. Guarino, J. Hajfler, and P. Günter, “Ion-sliced lithium niobate thin films for active photonic devices,” *Opt. Mater.* **31**, 1054–1058 (2009).
- Y. Jia, L. Wang, and F. Chen, “Ion-cut lithium niobate on insulator technology: Recent advances and perspectives,” *Appl. Phys. Rev.* **8**, 011307 (2021).
- G. Ulliac, V. Calero, A. Ndao, F. Baida, and M.-P. Bernal, “Argon plasma inductively coupled plasma reactive ion etching study for smooth sidewall thin film lithium niobate waveguide application,” *Opt. Mater.* **53**, 1–5 (2016).
- D. Zhu, L. Shao, M. Yu, R. Cheng, B. Desiatov, C. Xin, Y. Hu, J. Holzgrafe, S. Ghosh, A. Shams-Ansari *et al.*, “Integrated photonics on thin-film lithium niobate,” *Adv. Opt. Photonics* **13**, 242–352 (2021).

- <sup>39</sup>R. Krishna, T. Fan, A. H. Hosseinnia, X. Wu, Z. Peng, and A. Adibi, “Hybrid 3C-silicon carbide-lithium niobate integrated photonic platform,” *Opt. Express* **32**, 14555–14564 (2024).
- <sup>40</sup>L. Chen, Q. Xu, M. G. Wood, and R. M. Reano, “Hybrid silicon and lithium niobate electro-optical ring modulator,” *Optica* **1**, 112–118 (2014).
- <sup>41</sup>T. Vandekerckhove, T. Vanackere, J. De Witte, S. Cuyvers, L. Reis, M. Billet, G. Roelkens, S. Clemmen, and B. Kuyken, “Reliable micro-transfer printing method for heterogeneous integration of lithium niobate and semiconductor thin films,” *Opt. Mater. Express* **13**, 1984–1993 (2023).
- <sup>42</sup>Z. Wang, G. Chen, Z. Ruan, R. Gan, P. Huang, Z. Zheng, L. Lu, J. Li, C. Guo, K. Che *et al.*, “Silicon-lithium niobate hybrid intensity and coherent modulators using a periodic capacitively loaded traveling-wave electrode,” *ACS Photonics* **9**, 2668–2675 (2022).
- <sup>43</sup>S. Mookherjee, V. Mere, and F. Valdez, “Thin-film lithium niobate electro-optic modulators: To etch or not to etch,” *Appl. Phys. Lett.* **122**, 120501 (2023).
- <sup>44</sup>S. Shekhar, W. Bogaerts, L. Chrostowski, J. E. Bowers, M. Hochberg, R. Soref, and B. J. Shastri, “Road mapping the next generation of silicon photonics,” *Nat. Commun.* **15**, 751 (2024).
- <sup>45</sup>M. R. Billah, M. Blaicher, T. Hoose, P.-I. Dietrich, P. Marin-Palomo, N. Lindemann, A. Nestic, A. Hofmann, U. Troppenz, M. Moehle *et al.*, “Hybrid integration of silicon photonics circuits and InP lasers by photonic wire bonding,” *Optica* **5**, 876–883 (2018).
- <sup>46</sup>T. Vanackere, T. Vandekerckhove, L. Bogaert, M. Billet, S. Poelman, S. Cuyvers, J. Van Kerrebrouck, A. Moerman, O. Caytan, N. Singh *et al.*, “Heterogeneous integration of a high-speed lithium niobate modulator on silicon nitride using micro-transfer printing,” *APL Photonics* **8**, 086102 (2023).
- <sup>47</sup>L. Cao, A. Aboketaf, Z. Wang, and S. Preble, “Hybrid amorphous silicon (a-Si:H)-LiNbO<sub>3</sub> electro-optic modulator,” *Opt. Commun.* **330**, 40–44 (2014).
- <sup>48</sup>Y. Wang, Z. Chen, L. Cai, Y. Jiang, H. Zhu, and H. Hu, “Amorphous silicon-lithium niobate thin film strip-loaded waveguides,” *Opt. Mater. Express* **7**, 4018–4028 (2017).
- <sup>49</sup>A. N. R. Ahmed, S. Shi, A. Mercante, S. Nelan, P. Yao, and D. W. Prather, “High-efficiency lithium niobate modulator for K band operation,” *APL Photonics* **5**, 091302 (2020).
- <sup>50</sup>A. N. R. Ahmed, S. Shi, A. J. Mercante, and D. W. Prather, “High-performance racetrack resonator in silicon nitride—Thin film lithium niobate hybrid platform,” *Opt. Express* **27**, 30741–30751 (2019).
- <sup>51</sup>X. Han, Y. Jiang, A. Frigg, H. Xiao, P. Zhang, T. G. Nguyen, A. Boes, J. Yang, G. Ren, Y. Su *et al.*, “Mode and polarization-division multiplexing based on silicon nitride loaded lithium niobate on insulator platform,” *Laser Photonics Rev.* **16**, 2100529 (2022).
- <sup>52</sup>X. Xu, G. Ren, A. Dubey, T. Feleppa, X. Liu, A. Boes, A. Mitchell, and A. J. Lowery, “Phase retrieval of programmable photonic integrated circuits based on an on-chip fractional-delay reference path,” *Optica* **9**, 1401–1407 (2022).
- <sup>53</sup>L. Chang, Y. Li, N. Volet, L. Wang, J. Peters, and J. E. Bowers, “Thin film wavelength converters for photonic integrated circuits,” *Optica* **3**, 531–535 (2016).
- <sup>54</sup>T. Jin, J. Zhou, and P. T. Lin, “Mid-infrared electro-optical modulation using monolithically integrated titanium dioxide on lithium niobate optical waveguides,” *Sci. Rep.* **9**, 15130 (2019).
- <sup>55</sup>H. Nakanishi, H. Nakamura, and R. Goto, “High-electromechanical-coupling-coefficient surface acoustic wave resonator on Ta<sub>2</sub>O<sub>5</sub>/Al/LiNbO<sub>3</sub> structure,” *Jpn. J. Appl. Phys.* **49**, 07HD21 (2010).
- <sup>56</sup>P. Rabiei, J. Ma, S. Khan, J. Chiles, and S. Fathpour, “Heterogeneous lithium niobate photonics on silicon substrates,” *Opt. Express* **21**, 25573–25581 (2013).
- <sup>57</sup>X. Zhu, S. Nelan, A. J. Mercante, B. Shopp, P. Yao, S. Shi, and D. W. Prather, “Phase modulation using a titanium dioxide strip on lithium niobate,” *Opt. Mater. Express* **12**, 3296–3302 (2022).
- <sup>58</sup>M. Ma, M. Yuan, X. Zhou, H. Xiao, P. Cao, L. Cheng, T. G. Nguyen, A. Boes, G. Ren, Y. Su *et al.*, “Multimode waveguide bends in lithium niobate on insulator,” *Laser Photonics Rev.* **17**, 2200862 (2023).
- <sup>59</sup>Z. Yu, Y. Tong, H. K. Tsang, and X. Sun, “High-dimensional communication on etchless lithium niobate platform with photonic bound states in the continuum,” *Nat. Commun.* **11**, 2602 (2020).
- <sup>60</sup>J. J. Chakkoria, R. A. Aoni, A. Dubey, G. Ren, T. G. Nguyen, A. Boes, S. K. Selvaraja, and A. Mitchell, “Efficient poling-free wavelength conversion in thin film lithium niobate harnessing bound states in the continuum,” *Laser Photonics Rev.* **18**, 2301335 (2024).
- <sup>61</sup>Z. Yu, X. Xi, J. Ma, H. K. Tsang, C.-L. Zou, and X. Sun, “Photonic integrated circuits with bound states in the continuum,” *Optica* **6**, 1342–1348 (2019).
- <sup>62</sup>B. Lopez-Rodriguez, R. Van Der Kolk, S. Aggarwal, N. Sharma, Z. Li, D. Van Der Plaats, T. Scholte, J. Chang, S. Groblacher, S. F. Pereira *et al.*, “High-quality amorphous silicon carbide for hybrid photonic integration deposited at a low temperature,” *ACS Photonics* **10**, 3748–3754 (2023).
- <sup>63</sup>D. M. Lukin, M. A. Guidry, and J. Vučković, “Integrated quantum photonics with silicon carbide: Challenges and prospects,” *PRX Quantum* **1**, 020102 (2020).
- <sup>64</sup>S. Castelletto, A. Peruzzo, C. Bonato, B. C. Johnson, M. Radulaski, H. Ou, F. Kaiser, and J. Wrachtrup, “Silicon carbide photonics bridging quantum technology,” *ACS Photonics* **9**, 1434–1457 (2022).
- <sup>65</sup>D. M. Lukin, C. Dory, M. A. Guidry, K. Y. Yang, S. D. Mishra, R. Trivedi, M. Radulaski, S. Sun, D. Vercruyse, G. H. Ahn *et al.*, “4H-silicon-carbide-on-insulator for integrated quantum and nonlinear photonics,” *Nat. Photonics* **14**, 330–334 (2020).
- <sup>66</sup>P. Xing, D. Ma, L. C. Kimerling, A. M. Agarwal, and D. T. Tan, “High efficiency four wave mixing and optical bistability in amorphous silicon carbide ring resonators,” *APL Photonics* **5**, 076110 (2020).
- <sup>67</sup>P. Xing, D. Ma, K. J. Ooi, J. W. Choi, A. M. Agarwal, and D. Tan, “CMOS-compatible PECVD silicon carbide platform for linear and nonlinear optics,” *ACS Photonics* **6**, 1162–1167 (2019).
- <sup>68</sup>L.-Y. S. Chang, H. Nejadriahi, S. Pappert, and P. K. Yu, “Demonstration of DC Kerr effect induced high nonlinear susceptibility in silicon rich amorphous silicon carbide,” *Appl. Phys. Lett.* **120**, 071107 (2022).
- <sup>69</sup>N. Sharma, Z. Li, B. Lopez-Rodriguez, J. Vrugt, S. H. van der Waal, L. Li, R. van der Kolk, P. J. Poole, D. Dalacu, and I. Esmaeil Zadeh, “Design and validation of a-SiC/SiN hybrid photonic platform for integrated quantum photonics,” *Mater. Quantum Technol.* **4**, 035401 (2024).
- <sup>70</sup>Y. Lu, X. Shi, A. Ali Afridi, Y. Wang, V. Tabouret, D. Chaussende, K. Rot-twitz, and H. Ou, “Strong third-order nonlinearity in amorphous silicon carbide waveguides,” *Opt. Lett.* **49**, 4389–4392 (2024).
- <sup>71</sup>I. E. Zadeh, A. W. Elshaari, K. D. Jons, A. Fognini, D. Dalacu, P. J. Poole, M. E. Reimer, and V. Zwiller, “Deterministic integration of single photon sources in silicon based photonic circuits,” *Nano Lett.* **16**, 2289–2294 (2016).
- <sup>72</sup>Z. Li, B. Lopez-Rodriguez, N. Sharma, and I. Esmaeil-Zadeh, “Heterogeneous interconnection of low-loss and dense material platforms using adiabatic tapering coupler,” *EPJ Web Conf.* **287**, 01014 (2023).
- <sup>73</sup>B. Lopez-Rodriguez, N. Sharma, Z. Li, R. van der Kolk, J. van der Boom, T. Scholte, J. Chang, S. Groblacher, and I. E. Zadeh, “Magic silicon dioxide for widely tunable integrated photonics,” *arXiv:2407.08480* (2024).
- <sup>74</sup>Y. Sun, W. Shin, D. A. Laleyan, P. Wang, A. Pandey, X. Liu, Y. Wu, M. Soltani, and Z. Mi, “Ultra-high Q microring resonators using a single-crystal aluminum-nitride-on-sapphire platform,” *Opt. Lett.* **44**, 5679–5682 (2019).
- <sup>75</sup>A. Milton and W. Burns, “Mode coupling in optical waveguide horns,” *IEEE J. Quantum Electron.* **13**, 828–835 (1977).
- <sup>76</sup>A. R. Nelson, “Coupling optical waveguides by tapers,” *Appl. Opt.* **14**, 3012–3015 (1975).
- <sup>77</sup>J. P. Salvestrini, L. Guilbert, M. Fontana, M. Abarkan, and S. Gille, “Analysis and control of the DC drift in LiNbO<sub>3</sub> based Mach-Zehnder modulators,” *J. Lightwave Technol.* **29**, 1522–1534 (2011).
- <sup>78</sup>H. Nagata, N. O’Brien, W. Bosenberg, G. Reiff, and K. Voisine, “DC-voltage-induced thermal shift of bias point in LiNbO<sub>3</sub> optical modulators,” *IEEE Photonics Technol. Lett.* **16**, 2460–2462 (2004).
- <sup>79</sup>S. Sun, M. He, M. Xu, S. Gao, Z. Chen, X. Zhang, Z. Ruan, X. Wu, L. Zhou, L. Liu *et al.*, “Bias-drift-free Mach-Zehnder modulators based on a heterogeneous silicon and lithium niobate platform,” *Photonics Res.* **8**, 1958–1963 (2020).
- <sup>80</sup>O. T. Celik, N. Yousry Ammar, T. Park, H. S. Stokowski, K. K. Multani, A. Y. Hwang, S. Gyger, Y. Guo, M. M. Fejer, and A. H. Safavi-Naeini, “Roles of temperature, materials, and domain inversion in high-performance, low-bias-drift thin film lithium niobate blue light modulators,” *Opt. Express* **32**, 36160–36170 (2024).
- <sup>81</sup>A. Shams-Ansari, G. Huang, L. He, Z. Li, J. Holzgrafe, M. Jankowski, M. Churraev, P. Kharel, R. Cheng, D. Zhu *et al.*, “Reduced material loss in thin-film lithium niobate waveguides,” *APL Photonics* **7**, 081301 (2022).